Supplementary Information

Itinerant and topological excitations in a honeycomb spiral spin liquid

Yuqian Zhao, Xuping Yao, Xun Chen, Zongtang Wan, Zhaohua Ma, Xiaochen Hong & Yuesheng Li

Supplementary Note 1. Thermal conductivity and thermal Hall effect measurements

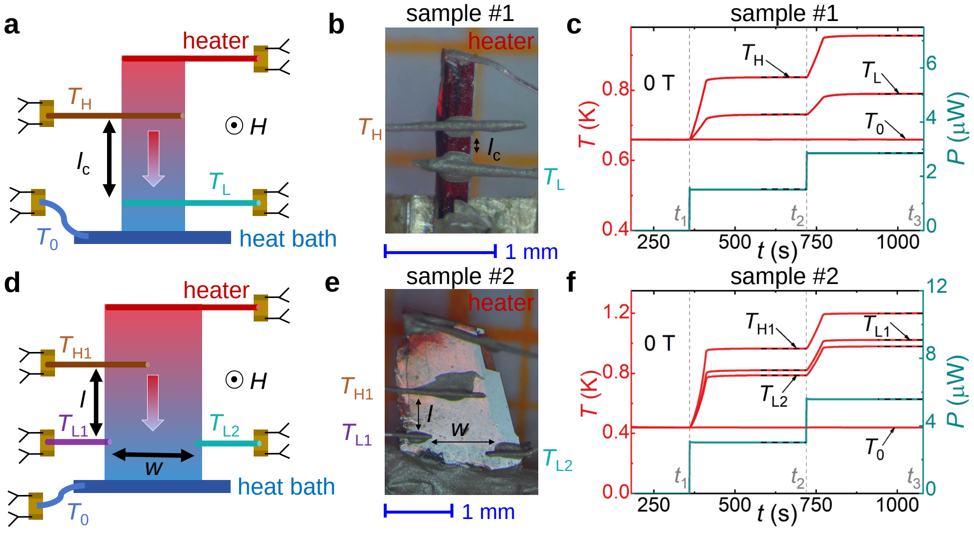

Supplementary Fig. 1 | **Samples #1 and #2. a**,**d**, Schematic diagrams of the thermal conductivity and thermal Hall effect measurement setups, respectively. **b**,**e**, Single-crystal samples #1 and #2 of GdZnPO used for the thermal conductivity and thermal Hall effect measurements. **c**,**f**, Temperature readings from thermometers and heater power measurements for samples #1 and #2 during the collection of two representative data points shown elsewhere. The dashed horizontal lines indicate the average values used to evaluate the longitudinal thermal conductivity and thermal Hall conductivity. Two different heating powers were applied at each temperature T_0 to test the reliability of our experimental setup (see text below).

We conducted longitudinal thermal conductivity and thermal Hall conductivity measurements on four as-grown GdZnPO crystals (#1-#4), as shown in Supplementary Figs. 1 and 2. The back-scattering Laue x-ray diffraction (XRD; detector: LAUESYS_V_674, Photonic Science & Engineering Ltd) patterns from the upper surfaces of these samples displayed sharp reflections (see Supplementary Fig. 3), indicating high crystallization quality. The XRD results also confirmed that the longest crystal directions were along [110] in the ab plane, ensuring the heat current predominantly flowed along this direction, with the magnetic field applied along the c axis for all samples. The average cross-section areas of the heat flow (thickness × full width) were measured using a microscope: A = 0.17×0.29, 0.06×1.63, 0.06×0.83, and 0.03×1.74

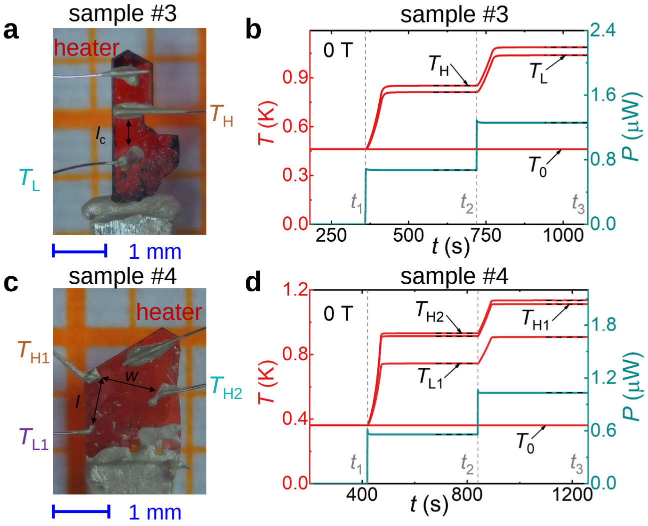

Supplementary Fig. 2 | **Samples #3 and #4. a**,**c**, Single-crystal samples #3 and #4 of GdZnPO used for thermal conductivity and thermal Hall effect measurements, respectively. **b**,**d**, Temperature readings from thermometers and heater power measurements for samples #3 and #4 during the collection of two representative data points shown elsewhere. The dashed horizontal lines indicate the average values used to evaluate the longitudinal thermal conductivity and thermal Hall conductivity. Two different heating powers were applied at each temperature T_0 to test the reliability of our experimental setup (see text below).

mm^2 for samples #1, #2, #3, and #4, respectively. Silver wires to the thermometers and a chip resistance heater were attached to the sample surfaces with silver paint (Supplementary Figs. 1 and 2), guiding the heat flow approximately along [110]. The measured distances between the temperature sensors were as follows: between T_{H} and T_{L} along the heat flow, l_{c} = 0.18 mm (Supplementary Fig. 1b) and 0.49 mm (Supplementary Fig. 2a) for samples #1 and #3, respectively; between T_{H1} and T_{L1} along the heat current, l = 0.47 mm (Supplementary Fig. 1e) and 1.01 mm (Supplementary Fig. 2c) for samples #2 and #4, respectively. The distances perpendicular to the heat current were w = 1.05 mm between T_{L2} and T_{L1} for sample #2 (Supplementary Fig. 1e), and 1.26 mm between T_{H2} and T_{H1} for sample #4 (Supplementary Fig. 2c).

All RuO$_2$ chip thermometers (T_{H}, T_{L}, T_{H1}, T_{L1}, T_{H2}, and T_{L2}; RX-102A-BR, LakeShore) were *in situ* calibrated against a reference thermometer (T_0, RX-102B-RS-0.02B, LakeShore, calibrated down to 18 mK) prior to each measurement. Calibration was performed under the temperature range (0.03 to 2 K) and magnetic field conditions (-12 to 12 T), by turning off the heater power (P = 0) at $t < t_1$ (Supplementary Figs. 1c,f and 2b,d). To ensure a high signal-to-noise ratio, all thermometers were measured using Lakeshore Model 372 resistance bridges/temperature controllers equipped with specially designed internal

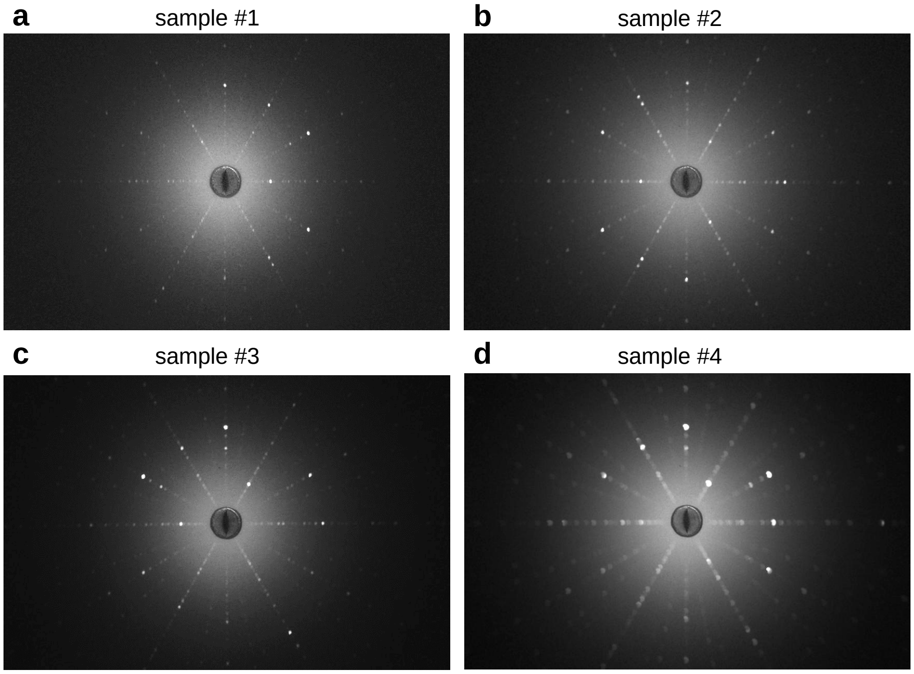

Supplementary Fig. 3 | Laue x-ray diffraction (XRD) patterns. a-d, Patterns measured on the upper surfaces of samples #1-#4 following thermal conductivity and thermal Hall effect measurements. All Laue XRD measurements were performed sequentially under identical conditions: tungsten target (20 kV, 15 mA), 400 s exposure, and a consistent sample-detector distance.

lock-in amplifiers. The longitudinal thermal conductivity (κ_{xx}) and thermal Hall conductivity (κ_{xy}) measurements were conducted using a standard four-wire steady-state method [1] for the elongated samples #1 and #3 (Supplementary Figs. 1c and 2b), and a five-wire steady-state method for the wider samples #2 and #4 (Supplementary Figs. 1f and 2d). Measurements were performed in high vacuum using a ^{3}He-^{4}He dilution refrigerator (KELMX-400, Oxford Instruments). The lower and higher power data were averaged over $(t_1 + t_2)/2 < t < t_2$ and $(t_2 + t_3)/2 < t < t_3$, respectively (Supplementary Figs. 1c,f and 2b,d), and are presented in Supplementary Figs. 4 and 5 as solid and open data points.

The longitudinal thermal resistivity and thermal Hall resistivity are defined as $\omega_{xx} = A\nabla_x T/P$ and $\omega_{xy} = A\nabla_y T/P$, respectively, where $\nabla_x T$ and $\nabla_y T$ denote the temperature gradients parallel and perpendicular to the heat flow. Typically, $|\nabla_y T|$ ($|\omega_{xy}|$) is significantly smaller than $\nabla_x T$ (ω_{xx}). Consequently, the longitudinal thermal conductivity is given by $\kappa_{xx} = \omega_{xx}/(\omega_{xx}^2 + \omega_{xy}^2) \approx P/(A\nabla_x T)$ and the thermal Hall conductivity by $\kappa_{xy} = \omega_{xy}/(\omega_{xx}^2 + \omega_{xy}^2) = \kappa_{xx}\nabla_y T/\nabla_x T$. For the elongated samples #1 and #3, $\nabla_x T = (T_{\mathrm{H}} - T_{\mathrm{L}})/l_{\mathrm{c}}$ and the sample temperature $T = (T_{\mathrm{H}} + T_{\mathrm{L}})/2$. For the wider crystals #2 and #4, $T = (T_{\mathrm{H1}} + T_{\mathrm{L1}})/2$, and $\nabla_x T(H)$ was calculated as $[(T_{\mathrm{H1}} - T_{\mathrm{L1}})|_H + (T_{\mathrm{H1}} - T_{\mathrm{L1}})|_{-H}]/(2l)$ to eliminate transverse responses

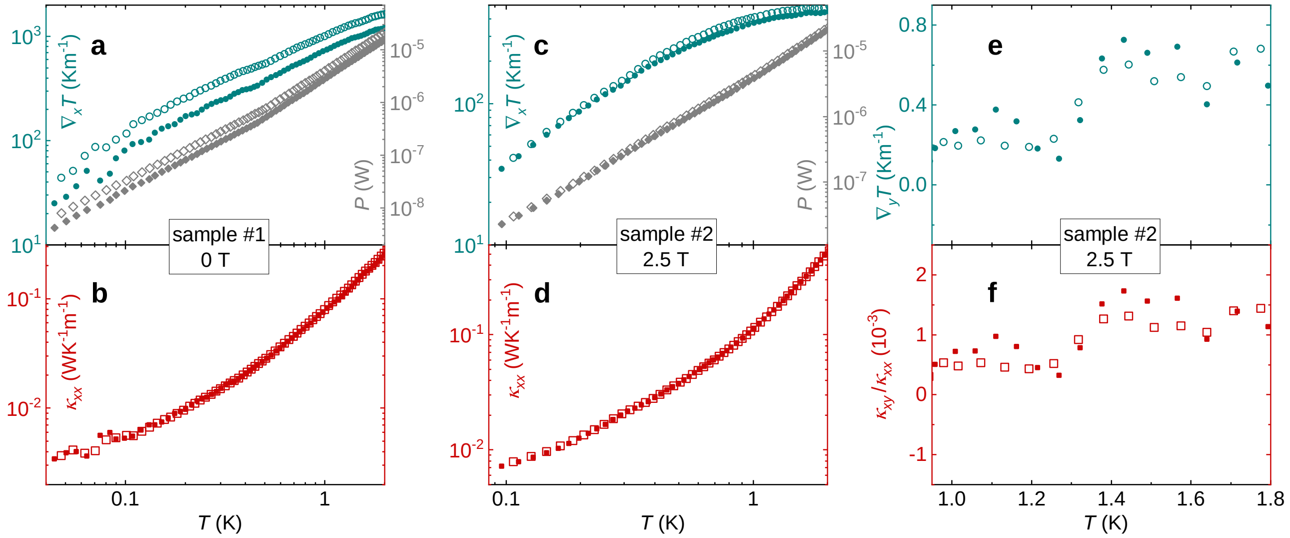

Supplementary Fig. 4 | Responses to heater power measured on samples #1 and #2. a, Heating power (P) applied to single-crystal sample #1 and the resulting temperature gradient along the heat flow ($\nabla_x T$). **b**, Thermal conductivity of sample #1, κ_{xx}. **c-f**, Raw thermal conductivity data measured at $\mu_0 H$ = 2.5 T on single-crystal sample #2. The heating power P is shown in **c**, and the corresponding temperature gradients parallel and perpendicular to the heat flow, $\nabla_x T$ and $\nabla_y T$, are shown in **c** and **e**, respectively. κ_{xx} (**d**) and κ_{xy}/κ_{xx} ($\equiv \nabla_y T/\nabla_x T$) (**f**) were measured on sample #2. Solid and open symbols represent lower and higher power data, respectively.

caused by contact misalignment (see Supplementary Figs. 1e and 2c), since $\nabla_x T$ is an even function of the applied magnetic field H. Similarly, we evaluated $\nabla_y T(H) = [(T_{\mathrm{L2}} - T_{\mathrm{L1}})|_H - (T_{\mathrm{L2}} - T_{\mathrm{L1}})|_{-H}]/(2w)$ and $[(T_{\mathrm{H2}} - T_{\mathrm{H1}})|_H - (T_{\mathrm{H2}} - T_{\mathrm{H1}})|_{-H}]/(2w)$ for samples #2 and #4, respectively, to eliminate longitudinal responses, given that $\nabla_y T$ is an odd function of H. For each sample and magnetic field, the measured κ_{xx} remained independent of the heater power P, indicating a good linear response and minimal heat leakage in our experimental setup (e.g., see Supplementary Figs. 4 and 5). Furthermore, the measured κ_{xy}/κ_{xx}, and thus κ_{xy}, also showed negligible dependence on P within a reasonable error range (see Supplementary Figs. 4 and 5).

For sample #2, the measured longitudinal thermal conductivity $\kappa_{xx} = Pl/[A(T_{\mathrm{H1}} - T_{\mathrm{L1}})]$ remains independent of the magnetic field's sign within a reasonable error range, as shown in Supplementary Fig. 6c, confirming that both κ_{xx} and $\nabla_x T$ are even functions of H. Conversely, the transverse-to-longitudinal temperature gradient ratio, $(T_{\mathrm{L2}} - T_{\mathrm{L1}})/(w\nabla_x T)$, clearly depends on the sign of H (see Supplementary Fig. 6a), reflecting the odd-function nature of $\nabla_y T$ due to $\kappa_{xy} \neq 0$. The absence of a noticeable linear-H dependence in the thermal Hall ratio κ_{xy}/κ_{xx} (see Supplementary Fig. 6b) may rule out a phonon-driven origin

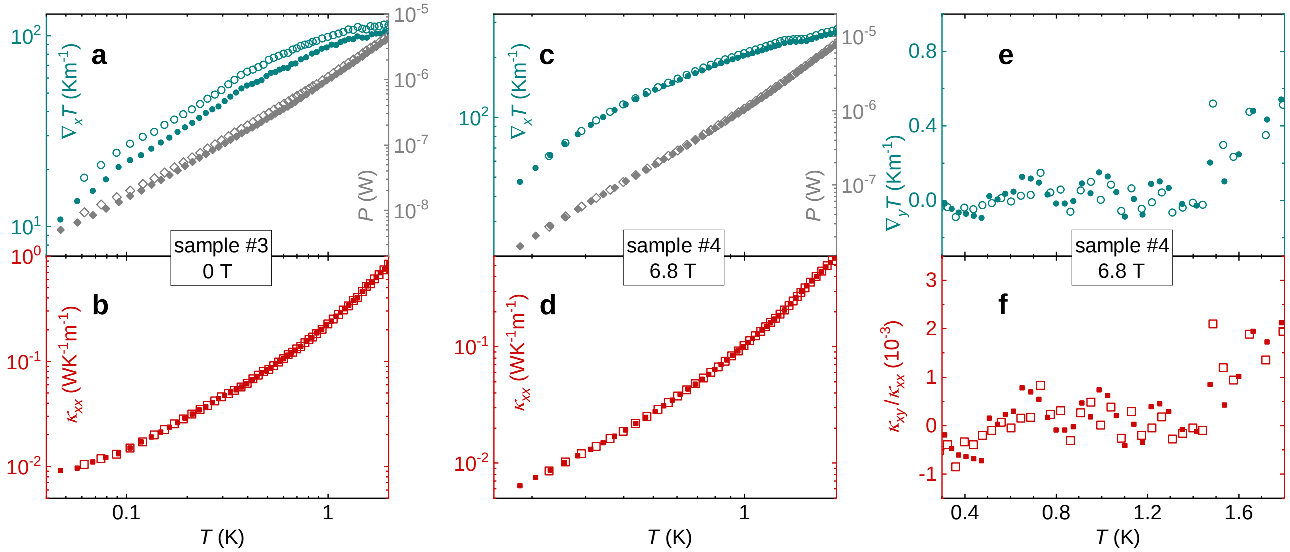

Supplementary Fig. 5 | Responses to heater power measured on samples #3 and #4. a, Heating power (P) applied to single-crystal sample #3 and the resulting temperature gradient along the heat flow ($\nabla_x T$). **b**, Thermal conductivity of sample #3, κ_{xx}. **c**-**f**, Raw thermal conductivity data measured at $\mu_0 H$ = 6.8 T on single-crystal sample #4. The heating power P is shown in **c**, and the corresponding temperature gradients parallel and perpendicular to the heat flow, $\nabla_x T$ and $\nabla_y T$, are shown in (**c**) and (**e**), respectively. κ_{xx} (**d**) and κ_{xy}/κ_{xx} ($\equiv \nabla_y T/\nabla_x T$) (**f**) were measured on sample #4. Solid and open symbols represent lower and higher power data, respectively.

for the thermal Hall effect [2]. While the crystal size of sample #4 is sufficient for thermal Hall conductivity measurements, its lower crystallization quality–evidenced by broader reflections in its Laue XRD pattern (see Supplementary Fig. 3)–distinguishes it from the other samples.

In insulators, crystal defects can introduce carriers, potentially reducing electrical resistivity [3]. The GdZnPO single crystals are good insulators with high resistivity, $\rho^{\mathrm{e}}_{xx} \geq 300\ \Omega$m, below 300 K (see Fig. 2 in the main text). Sample #4 shows a significantly smaller electric gap ($\sim$220 K) compared to the other samples ($\geq$330 K), confirming its inferior crystallization quality. As the temperature drops below $\sim$0.3 K, $\kappa^{\mathrm{m}}_{xx}/T$ for sample #4 shows a downturn with notably lower values (see Supplementary Fig. 7b), contrasting sharply with the other samples (e.g., Supplementary Fig. 7a). Additionally, the κ_{xy} signals from sample #4 are noticeably noisier than those from sample #2 (compare Supplementary Fig. 6d,e with Supplementary Fig. 6a,b). Nevertheless, even for sample #4, a nonzero $\kappa^{\mathrm{m}}_{xx}/T$ ($\sim$10 mWK^{-2}m^{-1}) is clearly observed at 0 T as $T \rightarrow 0$ K (see Supplementary Fig. 7b).

At selected magnetic fields, the thermal Hall conductivity (κ_{xy}) measured on sample #2 of GdZnPO can be analyzed similarly to Ref. [4]. Notably, at applied fields above $\sim$1.5 T, κ_{xy}/T increases with rising

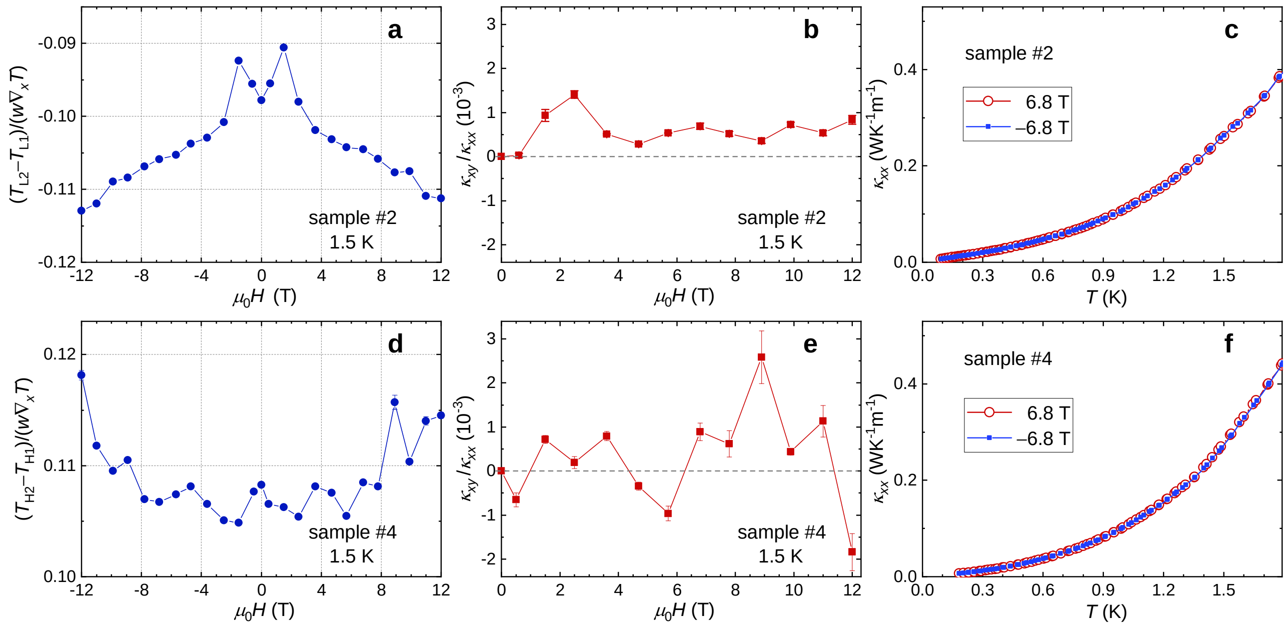

Supplementary Fig. 6 | Magnetic field dependence of longitudinal thermal conductivity and thermal Hall conductivity. **a**, Ratio of transverse to longitude temperature gradients, $(T_{\mathrm{L2}} - T_{\mathrm{L1}})/(w\nabla_x T)$, measured at 1.5 K on sample #2 (see Supplementary Fig. 1f). **b**, Thermal Hall ratios, κ_{xy}/κ_{xx} ($\equiv \nabla_y T/\nabla_x T$). **c**, Longitudinal thermal conductivity measured at 6.8 T and −6.8 T. **d-f**, Corresponding data measured on sample #4. In **a**,**b**,**d**,**e**, error bars, 1σ s.e.

temperature, reaching significant values above $\sim$1.2 K (see Supplementary Fig. 7c). These observations suggest that the excitations are bosonic. Uisng the two-flat-band approximation [4], the experimental κ_{xy} can be approximately fitted by,

$$\frac{\kappa_{xy}}{T} = \frac{k_{\mathrm{B}}^2 C_s}{h d_{\mathrm{inter}}}\left[\int_{\frac{\hbar\omega_1}{k_{\mathrm{B}}T}}^{\infty} \frac{x^2 e^x}{(e^x-1)^2}\mathrm{d}x - \int_{\frac{\hbar\omega_2}{k_{\mathrm{B}}T}}^{\infty} \frac{x^2 e^x}{(e^x-1)^2}\mathrm{d}x\right], \qquad (1)$$

where $\pm C_s$ is the Chern number of the lower (ω_1) or higher (ω_2) band, respectively, and d_{inter} = c/3 ($\sim$10.2 Å) is the average interlayer distance between neighboring GdO honeycomb layers in GdZnPO [5]. By fitting the data at 2.5, 4.7, 5.7, 8.9, 9.9, and 11 T (see Supplementary Fig. 7c), we obtained C_s = 1.18, 1.13, 0.99, 0.67, 1.21, and 1.13, $\hbar\omega_1$ = 5.4, 7.9, 6.8, 6.4, 6.5, and 6.9 K, $\hbar\omega_2$ = 16, 28, 27, 30, 10, and 28 K, respectively. The fitted C_s values are close to the integer value "1", supporting the validity of the two-flat-band model analysis [4]. The fitted values of $\hbar\omega_1$ and $\hbar\omega_2$ values are nearly an order of magnitude lower than the phonon energies, characterized by the Debye and Einstein temperatures, Θ_{D} and $\Theta_{\mathrm{E}n}$ (n = 1, 2, 3, see Supplementary Fig. 8). Additionally, κ_{xy}/κ_{xx} and κ_{xy}/T show no clear linear field dependence (see Supplementary Fig. 6b), which appears to contrast with the behavior observed in the phonon thermal Hall effect [2, 6, 7]. Thus, the thermal Hall conductivity observed at $\sim$1.5 K in GdZnPO (see Supplementary

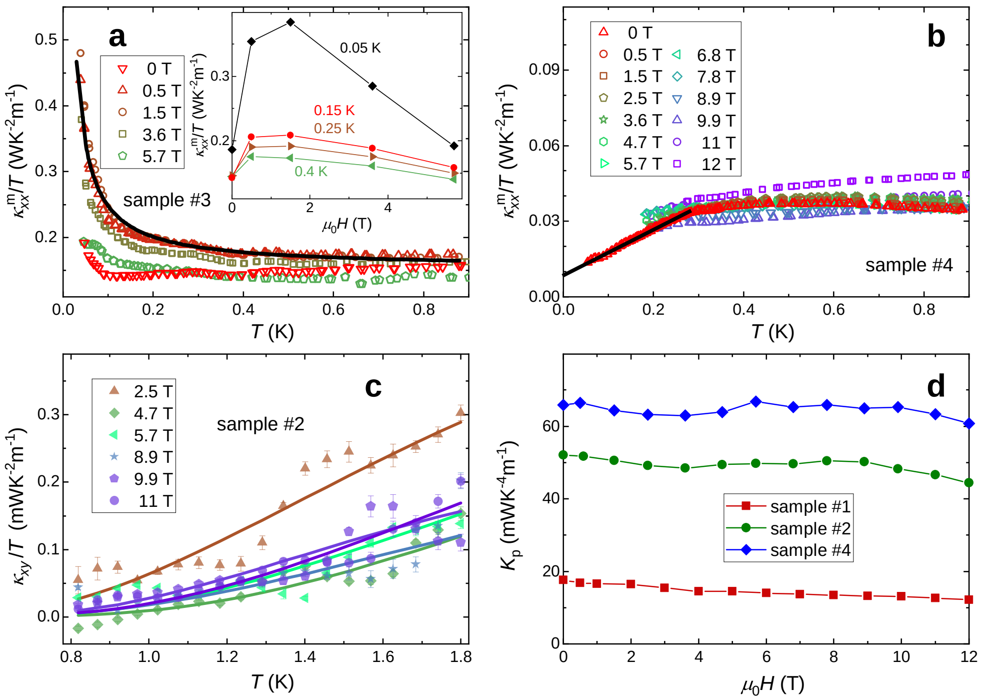

Supplementary Fig. 7 | Temperature dependence of longitudinal thermal conductivity and thermal Hall conductivity. a,**b**, Magnetic thermal conductivity (κ_{xx}^{m}) measured on samples #3 and #4, respectively. In **a**, the black line represents the low-field behavior $\kappa_{xx}^{\mathrm{m}} = \kappa_1 T + \kappa_0$, where both κ_1 and κ_0 are positive constants. The inset shows the field dependence of $\kappa_{xx}^{\mathrm{m}}/T$ for sample #3. In **b**, the straight line shows the low-temperature behavior of $\kappa_{xx}^{\mathrm{m}}/T$ at 0 T. **c**, Temperature dependence of the thermal Hall conductivity (κ_{xy}) measured on sample #2, with the colored lines showing the fits using Supplementary Eq. (1). **d**, Magnetic field dependence of phonon prefactor K_{p}. In **c**, error bars, 1σ s.e.

Figs. 6b and 7c) should predominantly originate from magnetic excitations.

Supplementary Note 2. Lattice specific heat

The magnetic specific heat of GdZnPO (see the main text) was obtained by subtracting the lattice contribution, estimated from the specific heat of the nonmagnetic reference compound YZnPO (Supplementary Fig. 8). The specific heat of YZnPO can be fitted using a Debye-Einstein model similar to that in Refs. [1, 8, 9],

$$C_{\mathrm{la}} = \frac{3w_0RT^3}{Z\Theta_{\mathrm{D}}^3}\int_0^{\frac{\Theta_{\mathrm{D}}}{T}}\frac{\xi^4e^{\xi}}{(e^{\xi}-1)^2}\mathrm{d}\xi + \frac{R}{ZT^2}\sum_{n=1}^{3}\frac{w_n\Theta_{\mathrm{E}n}^2e^{\frac{\Theta_{\mathrm{E}n}}{T}}}{(e^{\frac{\Theta_{\mathrm{E}n}}{T}}-1)^2}, \tag{2}$$

where $Z = 6$ represents the number of formulas per unit cell of YZnPO (or GdZnPO), and the weight factors $w_0 = 3$, $w_1 = 6$, $w_2 = 27$, $w_3 = 36$ are fixed ($w_0 + w_1 + w_2 + w_3 = 3\times4\times Z$) for simplicity. The fitted Debye

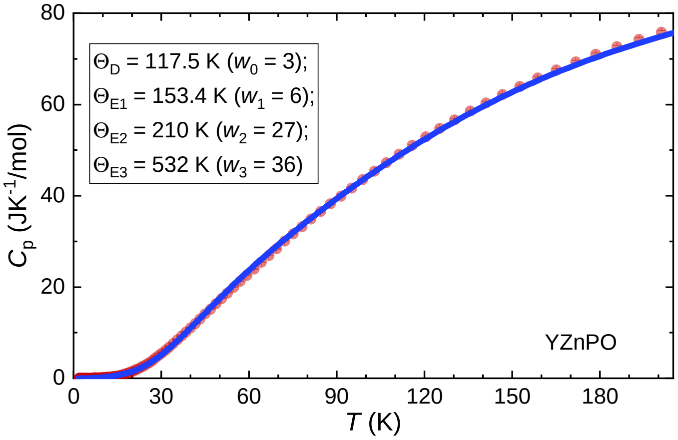

Supplementary Fig. 8 | Specific heat of the nonmagnetic reference compound YZnPO. The blue line shows the fit using the Debye-Einstein lattice model (see Supplementary Eq. (2)), with the fitted parameters listed. Error bars, 1σ s.e.

and Einstein temperatures, Θ_{D} and Θ_{En}, are listed in Supplementary Fig. 8. At $T \ll \Theta_{\mathrm{D}}$ (~117.5 K), the lattice specific heat (per mole formula) is proportional to T^3, $C_{\mathrm{la}} \simeq \frac{12\pi^4 RT^3}{5Z\Theta_{\mathrm{D}}^3}$ ($C_{\mathrm{la}}T^{-3} \simeq 1.997 \times 10^{-4}$ JK^{-4}/mol), where R = 8.314 JK^{-1}/mol is the gas constant.

The phonon thermal conductivity is given by $\kappa_{\mathrm{p}} \simeq \frac{C_{\mathrm{la}}\lambda_{\mathrm{p}}v_{\mathrm{p}}}{3N_{\mathrm{A}}V_0} \propto T^3$ at $T \ll \Theta_{\mathrm{D}}$, where λ_{p} is the phonon mean free path, $v_{\mathrm{p}} = \frac{k_{\mathrm{B}}\Theta_{\mathrm{D}}}{\hbar}(\frac{ZV_0}{6\pi^2})^{\frac{1}{3}} \sim$ 2,900 m/s is the phonon velocity, and $V_0 = \frac{\sqrt{3}a^2c}{2Z} \sim 6.76\times10^{-29}$ m^3/f.u. is the volume per formula. The lattice parameters are $a \sim$ 3.92 Å and $c \sim$ 30.5 Å in GdZnPO. By fitting the measured thermal conductivities with $\kappa_{xx}/T = (\kappa_{xx}/T)_0 + K_{\mathrm{p}}T^2$ in the range 0.9-1.8 K, we obtained the phonon prefactor $K_{\mathrm{p}} \sim \kappa_{\mathrm{p}}T^{-3} \sim$ 17.7, 52.1, 65.7, and 65.9 mWK^{-4}m^{-1}, for samples #1-#4, respectively (see the main text). This yields phonon mean free paths of $\lambda_{\mathrm{p}} \sim$ 4, 11, 14, and 14 μm. These values are smaller than yet comparable to the crystal thicknesses (which are significantly smaller than the widths in cross sections for all the samples, see above), indicating that λ_{p} may be affected by both crystal size and crystallization quality.

Supplementary Note 3. Linear spin-wave theory for the spiral spin liquid

Under a magnetic field (H) applied along the c axis, the S = 7/2 Hamiltonian of GdZnPO can be approximated as [5]

$$\mathcal{H} = J_1 \sum_{\langle j0,j1\rangle} \mathbf{S}_{j0}\cdot\mathbf{S}_{j1} + J_2 \sum_{\langle\langle j0,j2\rangle\rangle} \mathbf{S}_{j0}\cdot\mathbf{S}_{j2} + D\sum_{j0}(S_{j0}^z)^2 - \mu_0 H g\mu_{\mathrm{B}}\sum_{j0} S_{j0}^z, \tag{3}$$

where $J_1 \sim -0.39$ K and $J_2 \sim 0.57$ K denote the first ($\langle\ \rangle$) and second ($\langle\langle\ \rangle\rangle$) nearest-neighbor couplings, respectively, $D \sim 0.30$ K represents the easy-plane anisotropy, and $g \sim 2$ is the g factor. The combination of J_1 and J_2 induces spin frustration on the honeycomb lattice. At the classical level, the ground-state state of Supplementary Eq. (3) is expected to be a spiral spin liquid (SSL) [10], with

$$\mathbf{S}_j^A = S[\cos\psi\cos(\mathbf{Q}\cdot\mathbf{R}_j), \cos\psi\sin(\mathbf{Q}\cdot\mathbf{R}_j), \sin\psi] \ \text{ and} \tag{4}$$

$$\mathbf{S}_j^B = S[\cos\psi\cos(\mathbf{Q}\cdot\mathbf{R}_j+\phi), \cos\psi\sin(\mathbf{Q}\cdot\mathbf{R}_j+\phi), \sin\psi], \tag{5}$$

for spins on the sublattices A and B of the honeycomb lattice, respectively, where $\mathbf{Q} = h\mathbf{b}_1 + k\mathbf{b}_2$ is the ordering wave vector, $\mathbf{b}_1$ and $\mathbf{b}_2$ are the reciprocal lattice vectors, and $\mathbf{R}_j$ denotes the position vector of the j-th unit cell. Using this ansatz, we calculate the system's energy per site as

$$E = (D+\frac{3J_1}{2}+3J_2)S^2\sin^2\psi + h_\mathrm{Z}S\sin\psi + \frac{J_1S^2\cos^2\psi}{2}[\cos\phi+\cos(\phi-2\pi h)+\cos(\phi-2\pi h-2\pi k)]$$
$$+ J_2S^2\cos^2\psi[\cos(2\pi h)+\cos(2\pi k)+\cos(2\pi h+2\pi k)], \tag{6}$$

where $h_\mathrm{Z} = -\mu_0 H g\mu_\mathrm{B}$. By minimizing Supplementary Eq. (6), the angles ϕ and ψ are determined as $\cos\phi = \frac{f_1}{\sqrt{f_1^2+f_2^2}}$, $\sin\phi = \frac{f_2}{\sqrt{f_1^2+f_2^2}}$, and $\sin\psi = -\frac{h_\mathrm{Z}}{2S\eta}$. Here, $f_1 = 1 + \cos(2\pi h_\mathrm{G}) + \cos(2\pi h_\mathrm{G} + 2\pi k_\mathrm{G})$, $f_2 = \sin(2\pi h_\mathrm{G}) + \sin(2\pi h_\mathrm{G} + 2\pi k_\mathrm{G})$, and $\eta = D + \frac{3J_1}{2} + \frac{J_1^2}{8J_2} + \frac{9J_2}{2}$, along with the degenerate spiral contour,

$$\cos(2\pi h_\mathrm{G}) + \cos(2\pi k_\mathrm{G}) + \cos(2\pi h_\mathrm{G} + 2\pi k_\mathrm{G}) = \frac{1}{2}(\frac{J_1^2}{4J_2^2} - 3). \tag{7}$$

Using the ground state described in Supplementary Eqs. (4) and (5), a new spin coordinate system for $\mathbf{S}'$ is defined as

$$\mathbf{S}_j^A = R^z(\mathbf{Q}\cdot\mathbf{R}_j)R^y(\pi/2-\psi)\mathbf{S'}_j^A \ \text{ and} \tag{8}$$

$$\mathbf{S}_j^B = R^z(\mathbf{Q}\cdot\mathbf{R}_j+\phi)R^y(\pi/2-\psi)\mathbf{S'}_j^B, \tag{9}$$

where $R^\alpha(\theta)$ denotes a spin rotation operator about the α axis ($\alpha = y$ or z) by an angle θ. The spin Hamiltonian in Supplementary Eq. (3) is then expressed in the $\mathbf{S}'$ coordinate system as

$$\mathcal{H} = J_1\sum_{\langle j0,j1\rangle}\{[\sin^2\psi\cos(\mathbf{Q}\cdot\mathbf{R}_{j1}-\mathbf{Q}\cdot\mathbf{R}_{j0}+\phi)+\cos^2\psi]S_{j0}^{\prime x}S_{j1}^{\prime x}+\cos(\mathbf{Q}\cdot\mathbf{R}_{j1}-\mathbf{Q}\cdot\mathbf{R}_{j0}+\phi)S_{j0}^{\prime y}S_{j1}^{\prime y}$$
$$+[\cos^2\psi\cos(\mathbf{Q}\cdot\mathbf{R}_{j1}-\mathbf{Q}\cdot\mathbf{R}_{j0}+\phi)+\sin^2\psi]S_{j0}^{\prime z}S_{j1}^{\prime z}-\sin\psi\sin(\mathbf{Q}\cdot\mathbf{R}_{j1}-\mathbf{Q}\cdot\mathbf{R}_{j0}+\phi)(S_{j0}^{\prime x}S_{j1}^{\prime y}-S_{j0}^{\prime y}S_{j1}^{\prime x})\}$$
$$+J_2\sum_{\langle\langle j0,j2\rangle\rangle}\{[\sin^2\psi\cos(\mathbf{Q}\cdot\mathbf{R}_{j2}-\mathbf{Q}\cdot\mathbf{R}_{j0})+\cos^2\psi]S_{j0}^{\prime x}S_{j2}^{\prime x}+\cos(\mathbf{Q}\cdot\mathbf{R}_{j2}-\mathbf{Q}\cdot\mathbf{R}_{j0})S_{j0}^{\prime y}S_{j2}^{\prime y}$$
$$+[\cos^2\psi\cos(\mathbf{Q}\cdot\mathbf{R}_{j2}-\mathbf{Q}\cdot\mathbf{R}_{j0})+\sin^2\psi]S_{j0}^{\prime z}S_{j2}^{\prime z}-\sin\psi\sin(\mathbf{Q}\cdot\mathbf{R}_{j2}-\mathbf{Q}\cdot\mathbf{R}_{j0})(S_{j0}^{\prime x}S_{j2}^{\prime y}-S_{j0}^{\prime y}S_{j2}^{\prime x})\}$$
$$+D\sum_{j0}[\sin^2\psi(S_{j0}^{\prime z})^2+\cos^2\psi(S_{j0}^{\prime x})^2]+h_\mathrm{Z}\sin\psi\sum_{j0}S_{j0}^{\prime z}+(S_{j0}^{\prime x}S_{j1}^{\prime z}, S_{j0}^{\prime y}S_{j1}^{\prime z}, S_{j0}^{\prime x}S_{j2}^{\prime z}, S_{j0}^{\prime y}S_{j2}^{\prime z}\ \text{terms}). \tag{10}$$

We apply the Holstein-Primakoff transformation,

$$S_j^{\prime A+} \simeq \sqrt{2S} a_j, S_j^{\prime A-} \simeq \sqrt{2S} a_j^{\dagger}, S_j^{\prime Az} = S - a_j^{\dagger} a_j, \tag{11}$$

$$S_j^{\prime B+} \simeq \sqrt{2S} b_j, S_j^{\prime B-} \simeq \sqrt{2S} b_j^{\dagger}, S_j^{\prime Bz} = S - b_j^{\dagger} b_j, \tag{12}$$

where $a_j^{\dagger}$ and $b_j^{\dagger}$ (a_j and b_j) are bosonic creation (annihilation) operators, and $S_j^{\prime\pm} \equiv S_j^{\prime x} \pm i S_j^{\prime y}$. Performing the Fourier transformation, we derive the spin-wave Hamiltonian,

$$\mathcal{H}_{\rm sw} = \frac{1}{2} \sum_{\mathbf{k}} \Psi^{\dagger}(\mathbf{k}) \mathcal{H}(\mathbf{k}) \Psi(\mathbf{k}), \tag{13}$$

where $\Psi(\mathbf{k}) = [a(\mathbf{k}); b(\mathbf{k}); a^{\dagger}(-\mathbf{k}); b^{\dagger}(-\mathbf{k})]$. At $\mathbf{Q} = \mathbf{Q}_{\rm G} \equiv h_{\rm G}\mathbf{b}_1 + k_{\rm G}\mathbf{b}_2$, the Bogoliubov-de Gennes (BdG) Hamiltonian adopts the general form,

$$\mathcal{H}(\mathbf{k}) = \begin{bmatrix} \Xi(\mathbf{k}, \mathbf{Q}_{\rm G}) & \Pi(\mathbf{k}, \mathbf{Q}_{\rm G}) \\ \Pi^{*}(-\mathbf{k}, \mathbf{Q}_{\rm G}) & \Xi^{*}(-\mathbf{k}, \mathbf{Q}_{\rm G}) \end{bmatrix}, \tag{14}$$

with

$$\Xi(\mathbf{k}, \mathbf{Q}_{\rm G}) = \Xi^{0}(\mathbf{k}, \mathbf{Q}_{\rm G})\sigma_0 + \Xi^{x}(\mathbf{k}, \mathbf{Q}_{\rm G})\sigma_x + \Xi^{y}(\mathbf{k}, \mathbf{Q}_{\rm G})\sigma_y, \tag{15}$$

$$\Pi(\mathbf{k}, \mathbf{Q}_{\rm G}) = \Pi^{0}(\mathbf{k}, \mathbf{Q}_{\rm G})\sigma_0 + \Pi^{x}(\mathbf{k}, \mathbf{Q}_{\rm G})\sigma_x + \Pi^{y}(\mathbf{k}, \mathbf{Q}_{\rm G})\sigma_y. \tag{16}$$

Here, $\sigma_0 = \begin{bmatrix} 1 & 0 \\ 0 & 1 \end{bmatrix}$, $\sigma_x = \begin{bmatrix} 0 & 1 \\ 1 & 0 \end{bmatrix}$, and $\sigma_y = \begin{bmatrix} 0 & -i \\ i & 0 \end{bmatrix}$ represent Pauli matrices. Using Supplementary Eqs. (10)-(13), we determine all the prefactors in Supplementary Eqs. (15) and (16),

$$\begin{aligned} \Xi^{0} = & -J_1 S \sum_{\mathbf{R}_{01}} [\cos^2\psi \cos(\mathbf{Q}_{\rm G}\cdot\mathbf{R}_{01}+\phi)+\sin^2\psi] - J_2 S \sum_{\mathbf{R}_{02}} \{\sin\psi \sin(\mathbf{Q}_{\rm G}\cdot\mathbf{R}_{02}) \sin(\mathbf{k}\cdot\mathbf{R}_{02}) + \cos^2\psi \cos(\mathbf{Q}_{\rm G}\cdot\mathbf{R}_{02}) \\ & + \sin^2\psi - \frac{1}{2}[(1+\sin^2\psi)\cos(\mathbf{Q}_{\rm G}\cdot\mathbf{R}_{02}) + \cos^2\psi]\cos(\mathbf{k}\cdot\mathbf{R}_{02})\} + DS(1-3\sin^2\psi) - h_{\rm Z}\sin\psi, \end{aligned} \tag{17}$$

$$\Xi^{x} = \frac{J_1 S}{2} \sum_{\mathbf{R}_{01}} \{[(1+\sin^2\psi)\cos(\mathbf{Q}_{\rm G}\cdot\mathbf{R}_{01}+\phi)+\cos^2\psi]\cos(\mathbf{k}\cdot\mathbf{R}_{01}+\mathbf{k}\cdot\delta) - 2\sin\psi \sin(\mathbf{Q}_{\rm G}\cdot\mathbf{R}_{01}+\phi)\sin(\mathbf{k}\cdot\mathbf{R}_{01}+\mathbf{k}\cdot\delta)\}, \tag{18}$$

$$\Xi^{y} = \frac{J_1 S}{2} \sum_{\mathbf{R}_{01}} \{[(1+\sin^2\psi)\cos(\mathbf{Q}_{\rm G}\cdot\mathbf{R}_{01}+\phi)+\cos^2\psi]\sin(\mathbf{k}\cdot\mathbf{R}_{01}+\mathbf{k}\cdot\delta) + 2\sin\psi \sin(\mathbf{Q}_{\rm G}\cdot\mathbf{R}_{01}+\phi)\cos(\mathbf{k}\cdot\mathbf{R}_{01}+\mathbf{k}\cdot\delta)\}, \tag{19}$$

$$\Pi^{0} = \frac{J_2 S}{2} \cos^2\psi \sum_{\mathbf{R}_{02}} [1 - \cos(\mathbf{Q}_{\rm G}\cdot\mathbf{R}_{02})]\cos(\mathbf{k}\cdot\mathbf{R}_{02}) + DS\cos^2\psi, \tag{20}$$

$$\Pi^x = \frac{J_1 S}{2}\sum_{\mathbf{R}_{01}}[(\sin^2\psi - 1)\cos(\mathbf{Q}_\mathrm{G}\cdot\mathbf{R}_{01}+\phi)+\cos^2\psi]\cos(\mathbf{k}\cdot\mathbf{R}_{01}+\mathbf{k}\cdot\delta), \tag{21}$$

$$\Pi^y = \frac{J_1 S}{2}\sum_{\mathbf{R}_{01}}[(\sin^2\psi - 1)\cos(\mathbf{Q}_\mathrm{G}\cdot\mathbf{R}_{01}+\phi)+\cos^2\psi]\sin(\mathbf{k}\cdot\mathbf{R}_{01}+\mathbf{k}\cdot\delta), \tag{22}$$

where $\mathbf{R}_{01}$ = [0;0], [−1;0], [−1;−1] denote the vectors between unit cells for J_1, $\mathbf{R}_{02}$ = [1;0], [1;1], [0;1], [−1;0], [−1;−1], [0;−1] are the vectors between unit cells for J_2, and δ = [2/3;1/3] represents the vector from the A site to the B site within a unit cell. The BdG Hamiltonian in Supplementary Eq. (14) can be diagonalized using a paraunitary matrix $\mathcal{T}(\mathbf{k})$, which satisfies

$$\mathcal{T}^\dagger(\mathbf{k})\begin{bmatrix}1&0&0&0\\0&1&0&0\\0&0&-1&0\\0&0&0&-1\end{bmatrix}\mathcal{T}(\mathbf{k}) = \begin{bmatrix}1&0&0&0\\0&1&0&0\\0&0&-1&0\\0&0&0&-1\end{bmatrix}, \tag{23}$$

and

$$\mathcal{T}^\dagger(\mathbf{k})\mathcal{H}(\mathbf{k})\mathcal{T}(\mathbf{k}) = \begin{bmatrix}\hbar\omega_1(\mathbf{k})&0&0&0\\0&\hbar\omega_2(\mathbf{k})&0&0\\0&0&\hbar\omega_1(-\mathbf{k})&0\\0&0&0&\hbar\omega_2(-\mathbf{k})\end{bmatrix}. \tag{24}$$

Here, $\hbar\omega_1(\mathbf{k})$ and $\hbar\omega_2(\mathbf{k})$ (see Supplementary Fig. 9) match exactly with the calculations performed using SpinW in MATLAB [11].

For each $\mathbf{Q}_\mathrm{G}$, there are two energy dispersions, $\hbar\omega_1(\mathbf{k},\mathbf{Q}_\mathrm{G})$ and $\hbar\omega_2(\mathbf{k},\mathbf{Q}_\mathrm{G})$, with $\omega_1 \leq \omega_2$, since each unit cell hosts two spins on the honeycomb lattice. When $h_\mathrm{Z} \leq 2S\eta$, ω_1 exhibits a zero gap at the Γ point ($\mathbf{k}$ = 0), while displaying a local minimum near the K point–an effect attributed to the easy-plane anisotropy ($D > 0$). Consequently, ω_1 near the Γ point predominantly influences the low-temperature thermodynamic properties due to the Bose-Einstein distribution.

Similar to the Debye specific-heat model, we first determine the maximum frequency ω_m by integrating over the wave vector $\mathbf{k}$ across the first Brillouin zone (FBZ) and integrating $\mathbf{Q}_\mathrm{G}$ along the degenerate spiral contour within the FBZ,

$$N(\frac{2}{\sqrt{3}})^{\frac{3}{2}}\int_{\mathbf{k},\mathbf{Q}_\mathrm{G}\in\mathrm{FBZ}}[\omega_1(\mathbf{k},\mathbf{Q}_\mathrm{G}) \leq \omega_\mathrm{m}]\mathrm{d}\mathbf{k}\mathrm{d}\mathbf{Q}_\mathrm{G} = 1, \tag{25}$$

where N ($\to\infty$) denotes the number of unit cells along the a or b axis (accounting for a total of $2N^2$ spins), and $|\mathbf{b}_1|$ = $|\mathbf{b}_2|$ = 1.

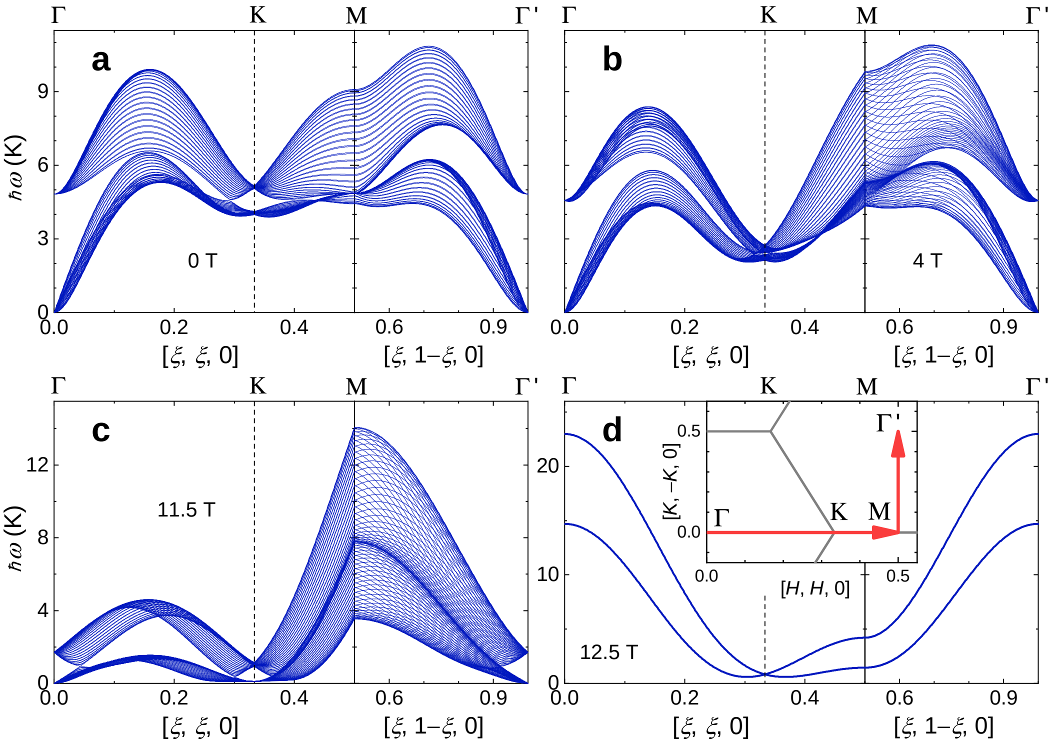

Supplementary Fig. 9 | Energy dispersions calculated using the linear spin-wave approximate at $\mu_0 H$ = 0 T (**a**), 4 T (**b**), 11.5 T (**c**), and 12.5 T (**d**). In **a**-**c**, the spin system is in the spiral spin liquid with $\mu_0 H < \mu_0 H_{\mathrm{c}}$ = $S[2D + 3J_1 + 9J_2 + J_1^2/(4J_2)]/(g\mu_{\mathrm{B}})$ ($\sim$ 12 T), while the system is fully polarized in **d**. The calculations are based on the determined spin Hamiltonian of GdZnPO [5]. The inset in **d** shows the high-symmetry directions with special **Q** points labeled, and the grey lines indicate Brillouin zone boundaries.

As a result, the low-temperature specific heat per mole of spins (see Supplementary Fig. 10a) is calculated as

$$C_{\mathrm{m}}^{\mathrm{cal}} = \frac{RN}{2}(\frac{2}{\sqrt{3}})^{\frac{3}{2}} \int_{\mathbf{k},\mathbf{Q}_{\mathrm{G}}\in\mathrm{FBZ}} [\omega_1(\mathbf{k},\mathbf{Q}_{\mathrm{G}}) \leq \omega_{\mathrm{m}}] \frac{(\frac{\hbar\omega_1}{k_{\mathrm{B}}T})^2 e^{\frac{\hbar\omega_1}{k_{\mathrm{B}}T}}}{(e^{\frac{\hbar\omega_1}{k_{\mathrm{B}}T}} - 1)^2} \mathrm{d}\mathbf{k}\mathrm{d}\mathbf{Q}_{\mathrm{G}}. \tag{26}$$

As $N \to \infty$, $\omega_{\mathrm{m}} \to 0$, making the low-temperature $C_{\mathrm{m}}^{\mathrm{cal}}$ predominantly influenced by the zero-energy excitations along the spiral contour, as shown in Supplementary Fig. 10a. Furthermore, we calculate the low-temperature magnon thermal conductivity (see Supplementary Fig. 10b) along the [110] direction using the relaxation approximation [12],

$$\kappa_{xx}^{\mathrm{cal}} = \frac{k_{\mathrm{B}}N}{2V_0}(\frac{2}{\sqrt{3}})^{\frac{3}{2}} \int_{\mathbf{k},\mathbf{Q}_{\mathrm{G}}\in\mathrm{FBZ}} [\omega_1(\mathbf{k},\mathbf{Q}_{\mathrm{G}}) \leq \omega_{\mathrm{m}}] \frac{(\frac{\hbar\omega_1}{k_{\mathrm{B}}T})^2 e^{\frac{\hbar\omega_1}{k_{\mathrm{B}}T}}}{(e^{\frac{\hbar\omega_1}{k_{\mathrm{B}}T}} - 1)^2} (\frac{\mathrm{d}\omega_1}{\mathrm{d}k})_{[110]}^2 \tau \mathrm{d}\mathbf{k}\mathrm{d}\mathbf{Q}_{\mathrm{G}}, \tag{27}$$

where $v(\mathbf{k} \parallel [110])$ = $(\frac{\mathrm{d}\omega_1}{\mathrm{d}k})_{[110]}$ represents the magnon group velocity along the [110] direction. The relaxation time τ is assumed to be independent of the wave vector, temperature, and magnetic field [12].

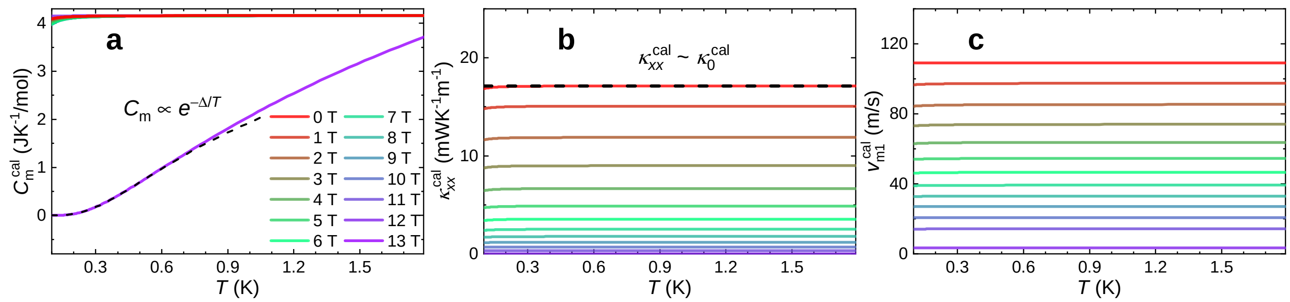

Supplementary Fig. 10 | Low-temperature specific heat, thermal conductivity, and mean magnon velocity calculated using the linear spin-wave approximation for GdZnPO. a, Specific heat (C_m), with the dashed black line showing the gap behavior, $C_\mathrm{m} \propto \exp(-\Delta/T)$, where $\Delta \sim 1$ K. **b**, Thermal conductivity (κ_{xx}) calculated with a fixed relaxation time $\tau = 10$ ps. The dashed black line represents the temperature-independent behavior at 0 T (i.e., $\kappa_{xx}^\mathrm{cal} \sim \kappa_0^\mathrm{cal} \sim$ const). **c**, Mean magnon velocity.

As $N \to \infty$, $\omega_\mathrm{m} \to 0$ makes the low-temperature κ_{xx}^cal predominantly influenced by zero-energy excitations along the spiral contour. Ideally, the magnon group velocity should be replaced by that of the zero-energy excitations. However, due to the absence of information on the presumably small velocities of zero-energy excitations, we instead used the considerably larger magnon velocity in Supplementary Eq. (27). The average number of magnons is given as

$$n_\mathrm{m} = N(\frac{2}{\sqrt{3}})^{\frac{3}{2}} \int_{\mathbf{k},\mathbf{Q}_\mathrm{G}\in\mathrm{FBZ}} \frac{\omega_1(\mathbf{k},\mathbf{Q}_\mathrm{G}) \leq \omega_\mathrm{m}}{e^{\frac{\hbar\omega_1}{k_\mathrm{B}T}} - 1} \mathrm{d}\mathbf{k}\mathrm{d}\mathbf{Q}_\mathrm{G}. \tag{28}$$

Consequently, the mean magnon velocity (see Supplementary Fig. 10c) is obtained as

$$v_\mathrm{m1}^\mathrm{cal} = \frac{N}{n_\mathrm{m}}(\frac{2}{\sqrt{3}})^{\frac{3}{2}} \int_{\mathbf{k},\mathbf{Q}_\mathrm{G}\in\mathrm{FBZ}} \frac{\omega_1(\mathbf{k},\mathbf{Q}_\mathrm{G}) \leq \omega_\mathrm{m}}{e^{\frac{\hbar\omega_1}{k_\mathrm{B}T}} - 1} |(\frac{\mathrm{d}\omega_1}{\mathrm{d}k})_{[110]}| \mathrm{d}\mathbf{k}\mathrm{d}\mathbf{Q}_\mathrm{G}. \tag{29}$$

The calculated $C_\mathrm{m}^\mathrm{cal}$, κ_{xx}^cal, and $v_\mathrm{m1}^\mathrm{cal}$, using Supplementary Eqs. (26), (27), and (29), exhibit negligible dependence on the system size N for $N \geq$ 10,000 above ~0.1 K. Therefore, we present the calculations for N = 30,000 in the main text and supplementary information. For $h_\mathrm{Z} < 2S\eta$ (i.e., $H < H_\mathrm{c}$, with $\mu_0 H_\mathrm{c} \sim 12$ T), the low-energy excitations of the spin system remain gapless at the Γ point, as shown in Supplementary Fig. 9a-c, and both $C_\mathrm{m}^\mathrm{cal}$ and κ_{xx}^cal remain large between 0.1 and 1.8 K. The low-T value of $C_\mathrm{m}^\mathrm{cal} \sim 4.2$ JK^{-1}/mol (~R/2) at $\mu_0 H < 12$ T is roughly consistent with classical Monte Carlo results (see the main text).

At $\mu_0 H > 12$ T, the spin system becomes fully polarized with gapped spin-wave excitations, lifting the degeneracy. The specific heat is then calculated as

$$C_\mathrm{m}^\mathrm{cal} = \frac{R}{2}(\frac{2}{\sqrt{3}}) \int_{\mathbf{k}\in\mathrm{FBZ}} [\frac{(\frac{\hbar\omega_1}{k_\mathrm{B}T})^2 e^{\frac{\hbar\omega_1}{k_\mathrm{B}T}}}{(e^{\frac{\hbar\omega_1}{k_\mathrm{B}T}} - 1)^2} + \frac{(\frac{\hbar\omega_2}{k_\mathrm{B}T})^2 e^{\frac{\hbar\omega_2}{k_\mathrm{B}T}}}{(e^{\frac{\hbar\omega_2}{k_\mathrm{B}T}} - 1)^2}] \mathrm{d}\mathbf{k}. \tag{30}$$

The calculated specific heat shows exponential behavior, $C_{\rm m}^{\rm cal} \propto \exp(-\Delta/T)$ with $\Delta \sim 1$ K at 13 T (see Supplementary Fig. 10a). At the same time, $\kappa_{xx}^{\rm cal}$ becomes negligible at high fields and low temperatures (see Supplementary Fig. 10b). As the applied field H increases, the gradient $\nabla_{\mathbf{k}}\omega_1$ around the Γ point in the reciprocal space ($\mathbf{k}$) decreases (see Supplementary Fig. 9a-c), leading to reductions in both $\kappa_{xx}^{\rm cal}$ (Supplementary Fig. 10b) and $v_{\rm m1}^{\rm cal}$ (Supplementary Fig. 10c).

Since $\kappa_{xx}^{\rm cal} \propto C_{\rm m}^{\rm cal}$, $\kappa_{xx}^{\rm cal}$ remains nearly constant, with $\kappa_{xx}^{\rm cal}$ = $\kappa_0^{\rm cal}$ $\sim$ 17.1 mWK^{-1}m^{-1} at τ = 10 ps and 0 T (see Supplementary Fig. 10b). Consequently, $\kappa_{xx}^{\rm cal}/T$ shows an upturn at $H < H_{\rm c}$ and low temperatures, consistent with experimental observations (see Supplementary Fig. 7a). Fitting the experimental $\kappa_{xx}^{\rm m}$ using $\kappa_{xx}^{\rm m}$ = $\kappa_1 T$+κ_0, we obtained $\kappa_0 \sim$ 6.3, 2.0, and 9.4 mWK^{-1}m^{-1} and $\kappa_1 \sim$ 47, 57, and 154 mWK^{-2}m^{-1} for samples #1, #2, and #3, respectively, at low applied magnetic fields. The experimental specific heat also shows similar behavior at low temperatures, with $C_{\rm m} \sim C_1 T$+C_0, where C_0 = 1.20(4) JK^{-1}/mol and C_1 = 2.7±0.2 JK^{-2}/mol [5]. Using these values, we calculated the experimental values, $\lambda_{\rm m0}v_{\rm m0} \sim 3N_{\rm A}V_0\kappa_0/C_0$ (ranging from 0.2 to 1.0 mm^{2}s^{-1}) and $\lambda_{\rm m1}v_{\rm m1} \sim 3N_{\rm A}V_0\kappa_1/C_1$ (ranging from 2 to 7 mm^{2}s^{-1}) at low fields for high-quality samples. Assuming $v_{\rm m1} \sim v_{\rm m1}^{\rm cal} \sim$ 110 ms^{-1}, we further estimate the mean free paths, $\lambda_{\rm m1}$ $\sim$ 200-600 Å, which is significantly smaller than the phonon mean free path $\lambda_{\rm p} \sim$ 4-14 μm.

Supplementary References

[1] Y. Zhao, Z. Ma, Z. He, H. Liao, Y.-C. Wang, J. Wang, and Y. Li, “Quantum annealing of a frustrated magnet,” Nat. Commun. **15**, 3495 (2024).

[2] C. Strohm, G. L. J. A. Rikken, and P. Wyder, “Phenomenological evidence for the phonon Hall effect,” Phys. Rev. Lett. **95**, 155901 (2005).

[3] J. Xiong, Y. Luo, Y. Khoo, S. Jia, R. J. Cava, and N. P. Ong, “High-field Shubnikov–de Haas oscillations in the topological insulator $\rm Bi_2Te_2Se$,” Phys. Rev. B **86**, 045314 (2012).

[4] P. Czajka, T. Gao, M. Hirschberger, P. Lampen-Kelley, A. Banerjee, N. Quirk, D. G. Mandrus, S. E. Nagler, and N. P. Ong, “Planar thermal Hall effect of topological bosons in the Kitaev magnet α-RuCl$_3$,” Nat. Mater. **22**, 36 (2023).

[5] Z. Wan, Y. Zhao, X. Chen, Z. Ma, Z. Li, Z. Ouyang, and Y. Li, “Spiral spin liquid in a frustrated honeycomb antiferromagnet: A single-crystal study of GdZnPO,” Phys. Rev. Lett. **133**, 236704 (2024).

[6] K. Sugii, M. Shimozawa, D. Watanabe, Y. Suzuki, M. Halim, M. Kimata, Y. Matsumoto, S. Nakatsuji, and M. Yamashita, “Thermal Hall effect in a phonon-glass $\rm Ba_3CuSb_2O_9$,” Phys. Rev. Lett. **118**, 145902 (2017).

[7] X. Li, B. Fauqué, Z. Zhu, and K. Behnia, “Phonon thermal Hall effect in strontium titanate,” Phys. Rev. Lett. **124**, 105901 (2020).

[8] J. Liu, L. Yuan, X. Li, B. Li, K. Zhao, H. Liao, and Y. Li, “Gapless spin liquid behavior in a kagome Heisenberg antiferromagnet with randomly distributed hexagons of alternate bonds,” Phys. Rev. B **105**, 024418 (2022).

[9] J. Liu, B. Liu, L. Yuan, B. Li, L. Xie, X. Chen, H. Zhang, D. Xu, W. Tong, J. Wang, and Y. Li, “Frustrat-

ed magnetism of the triangular-lattice antiferromagnets α-CrOOH and α-CrOOD," New J. Phys. **23**, 033040 (2021).

[10] K. Fujiwara, S. Kitamura, and T. Morimoto, "Thermal Hall responses in frustrated honeycomb spin systems," Phys. Rev. B **106**, 035113 (2022).

[11] S. Toth and B. Lake, "Linear spin wave theory for single-Q incommensurate magnetic structures," J. Phys.: Condens. Matter **27**, 166002 (2015).

[12] S. M. Rezende and J. C. López Ortiz, "Thermal properties of magnons in yttrium iron garnet at elevated magnetic fields," Phys. Rev. B **91**, 104416 (2015).